The Seismic Record
A journal of the Seismological Society of America

Supershear Rupture Along the Sagaing Fault Seismic Gap: The 2025 Myanmar Earthquake

OPEN ACCESS

Felipe Vera[1], Angela Carrillo-Ponce[1], Silvia Crosetto[1], Ehsan Kosari[1], Sabrina Metzger[1], Mahdi Motagh[1,2], Yanling Liang[1,5], Sen Lyu[1,2], Gesa Petersen[1], Joachim Saul[1], Henriette Sudhaus[3], Blanca Symmes-Lopetegui[1,6], Oo Than[4], Han Xiao[1], and Frederik Tilmann[*1,5]

Abstract

The 28 March 2025 M_w 7.7 Myanmar earthquake on the Sagaing fault caused widespread building collapses and over 3800 fatalities, as well as strong shaking in Bangkok. High-frequency backprojection very early on revealed an ~500 km rupture. Following a bilateral subshear propagation, the rupture accelerated southward to at least 5.3 km/s, reaching the stable supershear regime, as also confirmed by Mach-cone analysis with Love waves. Pixel tracking analysis from optical and radar imagery confirms the rupture length and indicates a peak surface offset of 5 m and average offsets of 3–4 m along the rupture zone. Pseudodynamic rupture inversion constrained by seismic waveforms and the radar-interferometric deformation field indicates ~4 m slip over ~15 km depth range. The earthquake yielded unusually few aftershocks; its supershear rupture likely released most of the accumulated stress. It appears that the rupture almost certainly broke the Sagaing gap and very likely overlapped completely with the 1956 M 7.0 event. It may also have partially overlapped with the 1946 M 7.8 rupture zone in the north and the 1930 M 7.5 event in the south. Acceleration to supershear only started in the gap area, and the rupture decelerated and arrested after moving into the previously broken segment.

Cite this article as Vera, F., A. Carrillo-Ponce, S. Crosetto, E. Kosari, S. Metzger, M. Motagh, Y. Liang, S. Lyu, G. Petersen, J. Saul, et al. (2025). Supershear Rupture Along the Sagaing Fault Seismic Gap: The 2025 Myanmar Earthquake, *The Seismic Record*. **5**(**3**), 289–299, doi: 10.1785/0320250025.

Supplemental Material

Introduction

On 28 March 2025 at 06:20:54 UTC (12:54 p.m. local time), an M_w 7.7 strike-slip earthquake nucleated near Sagaing, a town near Mandalay—the second largest city in Myanmar. The first damage reports came from Bangkok, more than 1000 km from the epicenter, where a high-rise building collapsed, causing 89 fatalities. Reports from the hardest-hit areas in Myanmar emerged more slowly, revealing widespread destruction in Mandalay and the capital, Naypyitaw (about 250 km to the south), providing key observations of the extent of the earthquake. Although data remain incomplete, recent estimates from the AHA Centre (ASEAN Coordinating Centre for Humanitarian Assistance) place fatalities at over 3800.

The Sagaing earthquake catastrophe vividly illustrates the rupture behavior of one of the longest, straightest strike-slip structures in the world, the Sagaing fault, underscoring the capacity of such faults to sustain high-speed ruptures over great lengths.

The Sagaing fault

The strike-slip Sagaing fault extends 1500 km from the eastern Himalayan syntaxis to the Andaman Sea spreading center (e.g., Curray, 2005; Fig. 1a), having accommodated ~200–460 km of

1. GFZ Helmholtz Centre for Geosciences, Potsdam, Germany, https://orcid.org/0000-0001-9284-2835 (FV); https://orcid.org/0000-0002-9720-7467 (AC-P); https://orcid.org/0000-0002-5584-1929 (SC); https://orcid.org/0000-0002-1052-4997 (EK); https://orcid.org/0000-0002-0803-6599 (SM); https://orcid.org/0000-0001-7434-3696 (MM); https://orcid.org/0000-0001-9945-5053 (YL); https://orcid.org/0009-0004-1252-612X (SL); https://orcid.org/0000-0002-7138-0499 (GP); https://orcid.org/0000-0002-2381-7289 (JS); https://orcid.org/0009-0003-3069-4808 (BS-L); https://orcid.org/0000-0001-8727-8053 (HX); https://orcid.org/0000-0002-7439-8782 (FT); 2. Institute of Photogrammetry and GeoInformation, Leibniz Universität Hannover, Hannover, Germany; 3. Geophysical Institute (GPI), Karlsruhe Institute of Technology, Karlsruhe, Germany, https://orcid.org/0000-0001-6335-5798 (HS); 4. Department of Meteorology and Hydrology (DMH), Naypyitaw, Myanmar, https://orcid.org/0000-0001-8304-7557 (OT); 5. Institute of Geological Sciences, Freie Universität Berlin, Berlin, Germany; 6. Institute of Geosciences, University of Potsdam, Potsdam, Germany

*Corresponding author: tilmann@gfz.de

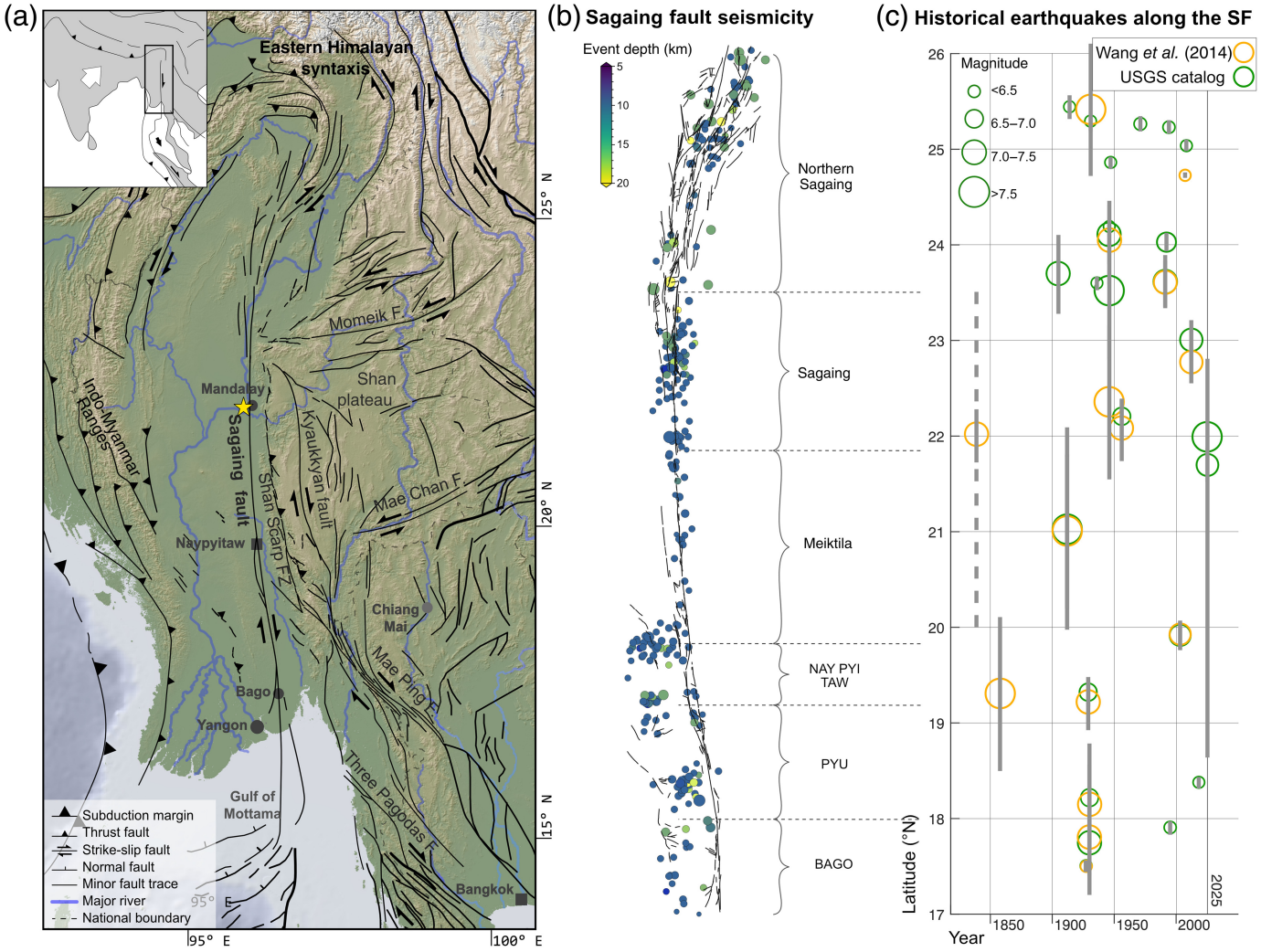

dextral offset since the Miocene (22–16 Ma; Searle *et al.*, 2007). Today, the 33–39 mm/yr India–Eurasia relative motion is mainly partitioned between the dextral Sagaing fault (up to 23–24 mm/yr; Tin *et al.*, 2022) and the Indo-Myanmar Ranges accretionary wedge.

Along its onshore central section, the Sagaing fault exhibits ≥700 km of continuous trace with only minor (≤1 km) step-overs, likely due to strain smoothing (Tun and Watkinson, 2017), making it the longest linear strike-slip fault worldwide (Robinson *et al.*, 2010). However, Wang *et al.* (2014) identified five segments (70–200 km long) based on geomorphology and seismicity (Fig. 1b), with potential maximum magnitudes of M_w 7–8. The earthquake record of the past 200 yr, characterized by multiple M 7+ events (Fig. 1c), reflects this segmentation.

Along the northern Sagaing segment, comprising four sub-parallel fault zones, four major earthquakes occurred since 1900: the 1991 M_w 6.9, 1946 M_w 7.7 (with M_w 7.3 foreshock), and 1931 M_w 7.6 events (Wang *et al.*, 2014). Southward, the Sagaing segment (~200 km) hosted the 1946 M_w 7.6–7.8 event and may have partially ruptured during the 2012 M_w 6.8 Thabeikkyin earthquake (Wang *et al.*, 2014; Tun and Watkinson, 2017), whereas its southern portion likely ruptured

Figure 1. Main fault traces of the Myanmar region and historical seismicity along the Sagaing fault. (a) Main fault systems in Myanmar and surrounding regions (after Tun and Watkinson, 2017; Crosetto *et al.*, 2019). The star marks the location of the 28 March 2025 earthquake. The top-left inset shows the location and wider tectonic context of the map. (b) Fault traces of the Sagaing fault (SF) in black (from Tun and Watkinson, 2017) and seismicity color coded by depth (U.S. Geological Survey [USGS]-National Earthquake Information Center [NEIC] earthquake catalog). (c) Historical earthquakes (from Wang *et al.*, 2014; Tun and Watkinson, 2017, and USGS-NEIC catalog for M 5+) plotted according to their year of occurrence and latitude, with the gray bar indicating the approximate rupture extent calculated according to the fault length–magnitude relationship proposed by Hurukawa and Maung Maung (2011).

in the 1956 M_w 7.0–7.1 earthquake (Hurukawa and Maung Maung, 2011). The 200 km long Meiktila segment, inactive for nearly two centuries (Wang *et al.*, 2014), is linked to the 1839 Amarapura earthquake, inferred to have ruptured both the Sagaing and Meiktila segments (Swe, 2013). The Meiktila segment, separating two clusters of large earthquakes to the north (1931–2012) and south (1929–1930), has therefore been regarded as a seismic gap (Hurukawa and Maung Maung, 2011; Wang *et al.*, 2014; Tun and Watkinson, 2017). The short (~70 km) Naypyitaw segment, with two parallel traces, last ruptured in the 1929 Swa earthquake ($M_w < 7$) (Tun and Watkinson, 2017). Farther south, the 130 km long Pyu segment likely fully ruptured during the 1930 Pyu earthquake (Hurukawa and Maung Maung, 2011; Wang *et al.*, 2014), whereas the 170 km long Bago segment (southern onshore termination) partially ruptured (~100 km) during the 1930 M_w 7.2–7.5 Pegu earthquake, producing ~3 m of right-lateral offset (Hurukawa and Maung Maung, 2011).

Despite partial ruptures (e.g., 2012 M_w 6.8 Thabeikkyin; (Tun and Watkinson, 2017) and multisegment events (e.g., 1839 Amarapura on the Sagaing–Meiktila segment; Wang *et al.*, 2014), recurrence intervals are estimated at decades for M_w 6.8–7.0 partial ruptures and 300–400 yr for M_w 7.7 full-segment ruptures.

Supershear ruptures

Strike-slip ruptures (so-called mode-II-cracks) typically propagate at sub-Rayleigh speeds but can accelerate beyond the shear-wave velocity to produce supershear ruptures (e.g., Robinson *et al.*, 2010). Supershear events occur most often on simple fault geometries under near-uniform stress-strength conditions (Bouchon *et al.*, 2010).

Backprojection imaging of coherent *P* waves at teleseismic arrays is a powerful tool for remotely characterizing rupture extent and complexity, including supershear propagation. Walker and Shearer (2009) confirmed supershear in the 2002 Denali earthquake, and Bao *et al.* (2019) revealed early and sustained supershear rupture during the 2018 Palu earthquake. Vera *et al.* (2024) used systematic multiarray backprojection to confirm supershear rupture in the Palu event and also the 2013 Craig earthquake offshore Alaska, and identified several other events that likely reached supershear velocities briefly.

In this study, we constrain the rupture geometry and kinematics using complementary approaches and find that the rupture extended ~500 km, initially propagating bilaterally at subshear speed and then accelerating to supershear during unilateral southward propagation. A pseudodynamic rupture (PDR) inversion reproduces the seismic and geodetic observations to first order with a simple rupture model, confirming the supershear character, which led to preferred radiation of long-period seismic energy in an oblique forward direction and may have contributed to the shaking in Bangkok.

Method Summary

Additional details for all methods can be found in the supplemental material, available to this article.

Constraining rupture kinematics from teleseismic data

We imaged the rupture process of the 2025 M_w 7.7 Myanmar earthquake using high-frequency *P*-wave backprojection (0.5–2.0 Hz). Following the multiarray method of Vera *et al.* (2024), we merged backprojections from four arrays (30°–90° epicentral distance) to enhance coverage and resolution (see Data and Resources). The arrays, formed from broadband seismic networks in Europe, Alaska, Japan (Hi-net), and Australia, provided broad azimuthal coverage (Fig. 2a, inset). Rupture length, propagation direction, and speed were estimated from the spatial–temporal distribution of emission points. We also compared intermediate-period Love waves from regional to teleseismic distances between the mainshock and an aftershock template to identify a possible Mach wave (Dunham and Bhat, 2008).

Coseismic displacement from satellite imagery

We generated coseismic displacement maps to constrain fault geometry and coseismic offsets using cross correlation (pixel-offset tracking) (Strozzi *et al.*, 2002) on mosaicked imagery from the radar satellite Sentinel-1 and optical satellite Sentinel-2. We also derived north–south and, by combining two view directions, along-strike surface displacements. Fault-perpendicular displacement profiles along the rupture allowed us to quantify surface fault offset in high spatial detail. The post-event satellite image acquisitions took place 8 and 11 days after the mainshock for Sentinel-1 data from descending and ascending orbits, respectively, and 2 and 4 days for Sentinel-2 data, potentially containing significant postseismic (afterslip) signals.

An Advanced Land Observation Satellite (ALOS)-2 ScanSAR interferogram, processed with the Interferometric Synthetic Aperture Radar (InSAR) Scientific Computing Environment (ISCE) software (Rosen *et al.*, 2012), which also accounts for ionospheric phase delays (Liang *et al.*, 2018), provided deformation data at intermediate distances (<200 km from the fault), in

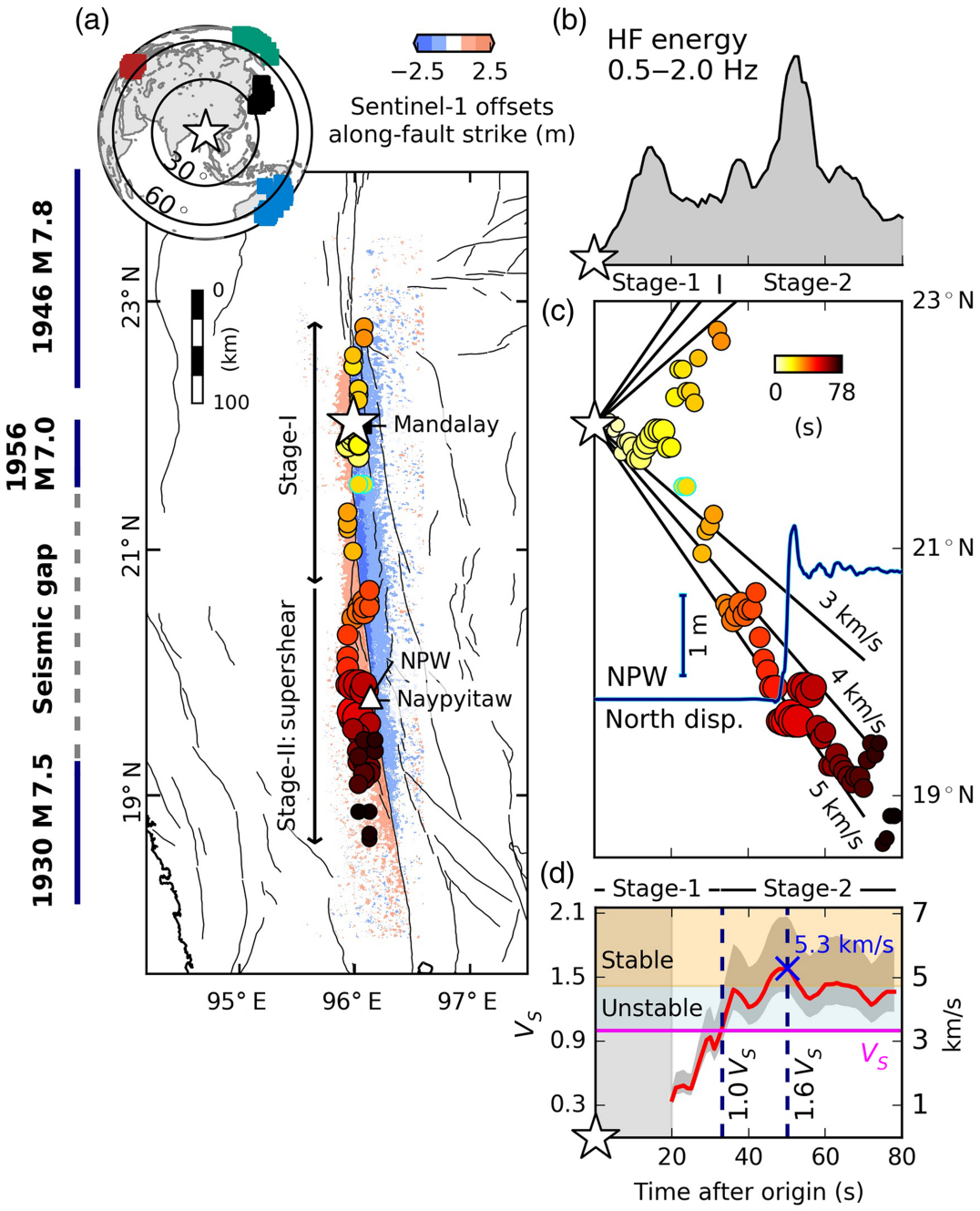

Figure 2. The 2025 M_w 7.7 Myanmar earthquake teleseismic backprojection (0.5–2.0 Hz). (a) Backprojected rupture evolution. Warm color-coded circles represent the tracked rupture front; colored by rupture time and scaled by the amplitude of high-frequency (HF) energy radiated. The blue-to-red background shows Sentinel-1 offsets along fault strike in the vicinity of the fault trace (see Fig. S2). The black solid lines indicate active faults from Zelenin *et al.* (2021). The inset figure indicates seismic arrays used for backprojection and the rupture lengths of historical seismicity, as inferred by Hurukawa and Maung Maung (2011). (b) Temporal variation of stacked high-frequency seismic energy. (c) Estimate of rupture speed. The black lines indicate reference slopes for 3, 4, and 5 km/s. In addition, the displacement trace at station NPW (blue; north component) as determined by double integration of the accelerometer trace (Lai *et al.*, 2025) is compared to the teleseismic rupture propagation. The baseline of this trace is at the latitude of the station, and the displacement offset occurs when the teleseismic emission points pass the station site. (d) Rupture velocity estimate as a function of the average shear wave speed (V_S). Because of the backprojection location uncertainties and the initial bilateral rupture phase, the first 20 s are excluded from the analysis. The rupture speed is shown relative to the average shear wave speed V_S = 5.3 km/s, and the upper and lower limits, based on the maximum and minimum shear wave speed along the fault, are indicated by gray shading.

which absolute displacements are too small for reliable pixel-offset tracking. For ALOS-2, the post-event satellite acquisitions took place only 42 hr after the mainshock.

Probabilistic inversion of the rupture mechanisms of main- and aftershocks

Probabilistic inversions of seismic waveforms were used to constrain Centroid Moment Tensors (CMTs) of the mainshock and aftershocks. Because of limited high-quality regional stations, we restricted the analysis to events with $M > 4$ from the GEOFON catalog. We used the *grond* inversion tool (Heimann *et al.*, 2018) to invert for (deviatoric) CMTs, using waveforms up to 10,000 km for the mainshock and up to 2,000 km for aftershocks. Because of data limitations, we did not interpret non-double-couple components. In total, 14 aftershocks and the mainshock were successfully inverted.

In addition, we performed a PDR inversion (Dahm *et al.*, 2021), fitting low-frequency broadband displacement (0.003–0.01 Hz) and regional acceleration (0.01–0.03 Hz) waveforms in long time windows from *P* onsets to a group velocity of 2.5 km/s. As a second data input, we use ALOS-2 coseismic displacements, which were subsampled using a quadtree approach following local deformation gradients (Jónsson *et al.*, 2002) after removing unreliable data, for example, phase unwrapping errors in the near-fault area (Fig. S3, right). Inversion results were complemented by 100 independent Bayesian bootstrapping data-weighting schemes to resolve uncertainties. Finite-fault length and location were constrained by the surface rupture mapped in Sentinel-2 coseismic pixel-offset data. Free parameters included nucleation point, rupture width (15–45 km), slip, and rupture-to-shear-wave velocity ratio (see Table S2). Strike, dip, and rake were constrained to −12° to +6°, 50°–90°, and 160°–220°, respectively. For the benefit of constraining our model simultaneously with seismic and geodetic observations, we simplified the fault geometry to a single, rectangular slip patch and ignored curvature, segmentation, and rupture speed variability. The long-period waveform filters accentuate surface waves, resulting in stable first-order estimates of the fault properties, whereas future higher-frequency segmented models may allow for a more precise estimate of the geometry and variability in slip.

Results

Supershear rupture: Back-projection imaging and Mach-Cone evidence

Teleseismic backprojection of the 2025 M_w 7.7 Myanmar earthquake revealed a ∼460 km rupture along the Sagaing fault, with supershear propagation sustained for over half its duration (Fig. 2). Emission points followed the surface trace of the main fault strand, with some scatter. Pixel tracking in satellite images further confirmed the rupture plane, as seen subsequently.

The resolution of backprojection is limited by array response, imperfect coherence, and biases from 3D heterogeneity. For the frequency band used here, typical errors range from 15 to 30 km (Vera *et al.*, 2024). The larger westward offset in the southern segment likely reflects that the array calibration, referenced to the event hypocenter, may be less suited for the southern end of the long rupture.

Initially (stage-1: 0–32 s), the rupture propagated bilaterally from the epicenter near Mandalay at subshear speeds, ∼85 km northward and ∼150 km southward. Although emissions appear primarily northward, southward propagation is evident from some emission points (Fig. 2a) and high-frequency snapshots (Movie S1). A secondary search grid identified additional southward emissions at 23–24 s (cyan points in Fig. 2a, Fig. S1), highlighting the bilateral nature of this phase. After ∼32 s, the northward branch terminated and the southward branch accelerated (stage-2: 33–78 s), reaching a peak velocity of at least 5.3 km/s around 50 s (Fig. 2d). The rupture then propagated southward another 225 km, reaching a total length of at least 460 km.

We relate the observed rupture speed to the average crustal shear speed from 0 to 25 km depth along three fault cross sections, extracted from the 3D shear-wave velocity model of Liang *et al.* (2023) (P1: 22° N; P2: 21° N; P3: 20° N; 95.5°–96.5° E), yielding $V_S = 3.4$ km/s. Consistent with supershear dynamics (Burridge *et al.*, 1979), the rupture first entered the unstable supershear regime (between V_S and $\sqrt{2}V_S$), then passed into the stable supershear range (between $\sqrt{2}V_S$ and V_P). This stage produced the strongest high-frequency radiation, peaking at 52 s near Naypyitaw (Fig. 2b,c), with peak rupture speed corresponding to $1.6V_S$. After 78 s, the scarcity of high-frequency emissions marks the end of the rupture.

Independent evidence for supershear rupture velocity comes from regional and teleseismic surface waves. In subshear ruptures, surface-wave arrivals from different parts of the fault reach stations at different times, with waves from the nucleation point arriving first. In fast ruptures, arrivals from all parts of the rupture coincide at specific take-off angles, forming a Mach cone, with the angle depending on the rupture-to-wave velocity ratio. Consequently, at azimuths near the Mach angle, high correlation is expected between the supershear mainshock and a smaller

event with a similar focal mechanism, even at periods much shorter than the rupture duration (e.g., Bao *et al.*, 2019). Here, we compared mainshock waveforms to those of the M_w 5.5 aftershock on 13 April 2025 at 02:24:57 UTC. To assess waveform similarity and amplitude scaling, we extracted Love waves in the 15–25 s band (see supplement for details).

Waveform similarity between the mainshock and chosen aftershock was markedly higher for stations within the Mach-cone azimuth range (Fig. 3a), confirming that the extended source resembled a point source at these stations. As the rupture was bilateral in stage-1 and transitioned to supershear only in stage-2, perfect waveform matching was not expected. Nonetheless, stations PALK and BBOO reached peak cross-correlation values of 0.87 and 0.83, respectively (Fig. 3b). Their amplitude ratios matched those predicted by the respective moments, confirming the Mach phase and validating the supershear rupture.

Finally, strong-motion data from station NPW (Naypyitaw; 2.6 km from the fault; Lai *et al.*, 2025) show a 1.6 m displacement step coincident with the rupture front in teleseismic backprojection (Fig. 2c, inset), confirming its tracking. The dominant fault-parallel motion indicates supershear speed at NPW (Bradley and Hubbard, 2025). The ~1.9 s rupture pulse duration matches estimates (1.3–1.7 s) from video recordings farther north (Bradley and Hubbard, 2025; Latour *et al.*, 2025).

Static displacement

Mapping of the surface fault rupture trace from Sentinel-1 (Fig. 2a), Sentinel-2 pixel correlation analysis (Fig. 4), and ALOS-2 ScanSAR imagery (Fig. S3) corroborated the rupture extent and propagation pattern inferred from teleseismic backprojection. The earthquake rupture followed a nearly linear and over 500 km long fault trace.

The coseismic offsets exhibited more than 4 m of relative fault-parallel surface slip along a 500-km-long rupture zone, slightly curved to the east (along-flight and along-strike direction: Fig. 2a, Fig. S2a,b; along north direction: Fig. 4a). Maximum along-strike offsets across the fault of ~5 m were observed near the epicenter (Fig. 4b,c, Fig. S2c). 50–100 km farther south, at 21.5° N, the offsets decrease to slightly over ~2 m to then increase again to 3–4 m in the southern part of the rupture (19°–21° N). At the northern end of the rupture, the offset tapered off faster than at the southern end. Note that the rupture ends often exhibit the highest vertical motion in strike-slip earthquakes, which remains undetected in pixel-offset measurements. At fault distances of 50 km, we still measured substantial north–south displacements of ~±1 m (Fig. 2a).

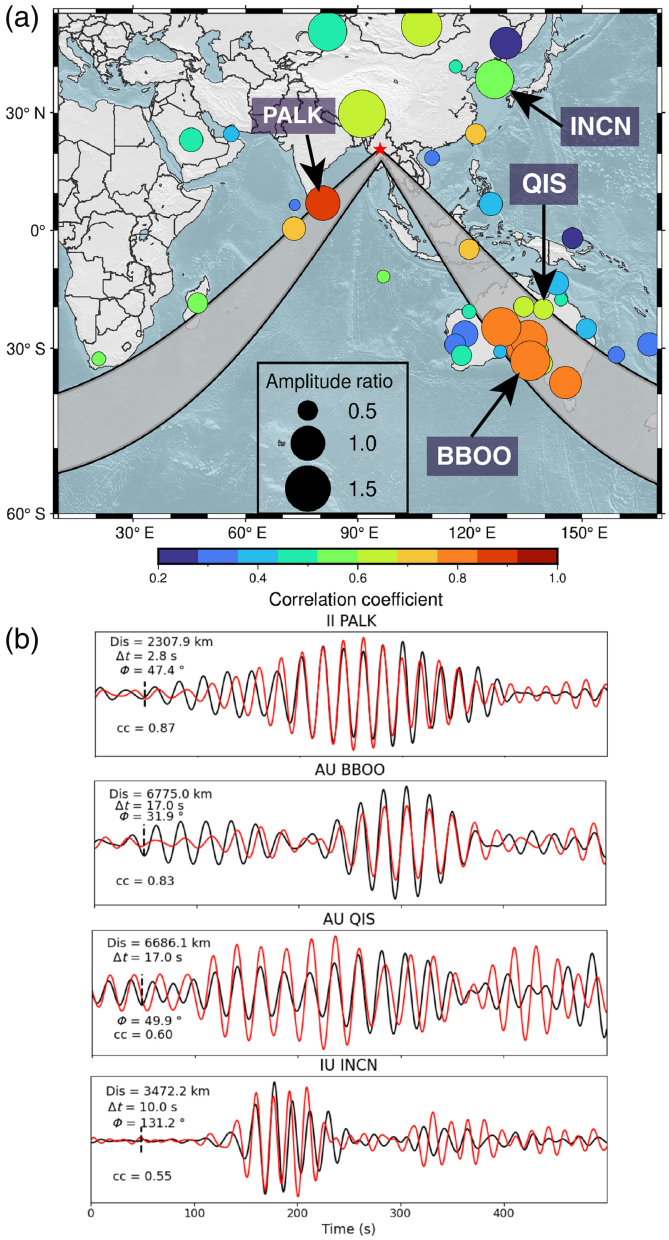

Figure 3. Mach-cone analysis using Love-wave propagation. (a) Seismic station locations (dots) and the aftershock epicenter (red star), with the Mach cone indicated by the shaded area. The dot color represents the correlation coefficient, and the dot size reflects the relative amplitude ratio. (b) Comparison of Love waveforms from the mainshock (black) and the aftershock (scaled by a factor of 1995; red). Stations II.PALK and AU.BBOO, near the Mach-cone angle, shows high correlation, and AU.QIS and IU.INCN, away from the cone, shows lower correlation.

The ALOS-2 coseismic displacement map showed minor atmospheric signals and coherent intermediate- and far-field displacements, with sharp line-of-sight offsets up to 1 m across the rupture (Fig. S3, left), despite the rather unfavorable look

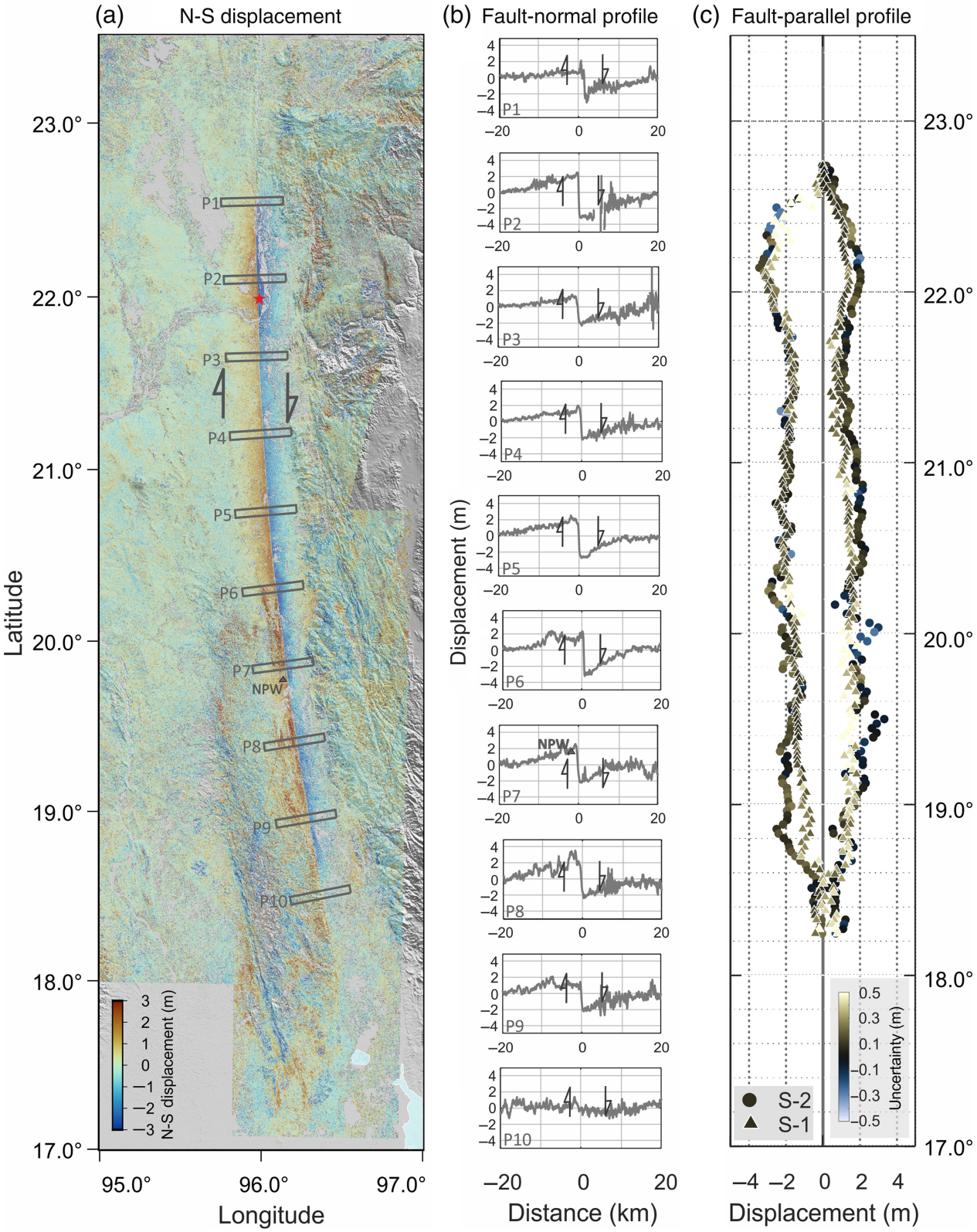

Figure 4. (a) North–south (N-S) displacement map from Sentinel-2 offset tracking. NPW indicates the NPW seismic station, also in (b) projected onto profile P7. The red star indicates the epicenter. (b) Multiple cross-fault profiles (marked in panel a) show the spatial variation of fault offset. (c) Comparison of fault-perpendicular surface NS-displacements along the rupture, derived from Sentinel-1 (S-1) and Sentinel-2 (S-2) offsets.

angle. West of the fault, the ground moved away from the satellite; east, it moved toward it.

Rupture dynamics: Pseudodynamic inversion

The PDR inversion uses a rectangular source model that ignores the slight fault curvature or segmentation. The final model constrained the nucleation point in the northernmost quarter of the fault, just 16 km northwest of the GEOFON epicenter (Fig. S4). The maximum-likelihood and mean PDR models agreed well within data resolution (see Table S4). The maximum-likelihood fault plane had a strike of −8° (mean 7° ± 2°), dip of 85° east (mean 82° ± 7°), and rake of 162° (mean 166° ± 4°). The PDR model confirms early bilateral propagation; during the first phase, the rupture advanced northward and southward. After ∼15 s (maximum likelihood) to 30 s (mean), rupture became unilateral to the south for at least 80 s, matching backprojection. Maximum slip reached 4.1 m (average 3.0 m), with an estimated stress drop of 3 MPa. The finite rupture model, assuming constant stress drop, robustly resolves rupture evolution and significant slip but does not capture heterogeneity in slip or rupture speed. Recovered slip-rate distributions imply high rupture speeds: $V_R/V_S = 1.17$ relative to $V_S = 3.5$ km/s, yielding an average rupture velocity of ∼4.35 km/s. These results corroborate the initial bilateral rupture and supershear-dominated southward propagation observed in backprojection and Mach-cone analyses. Because the PDR inversion does not allow a varying V_R/V_S, distinct phases of sub- or supershear cannot be resolved.

Moment tensor solutions of the aftershock activity

The Sagaing earthquake was followed by an unusually low number of aftershocks; only 18 events with $M \geq 4.5$ occurred in the four weeks after the mainshock (GEOFON catalog; see Data and Resources), compared to 72 aftershocks with $M \geq 4.5$ within four weeks after the two 2023 Türkiye events (M_w 7.7 and 7.6) and 28 earthquakes with $M \geq 4.7$ for the 2018 Palu earthquake in Sulawesi, Indonesia, which also exhibited supershear propagation, even though the event was smaller, M_w 7.5.

Using the available regional seismic station dataset, we derived CMT solutions for 14 aftershocks (Fig. 5). Most occurred on or near the Sagaing fault, with one event offset to the west (marked C in Fig. 5). Centroid location uncertainties from Bayesian bootstrapping ranged from <5 km to >20 km, making on-fault locations possible for nearly all events (see Tables T1 and T2). Event C's east–west error was only 5.4 km, confirming its off-fault location despite unmodeled 3D heterogeneity. Most mechanisms were strike slip, consistent with the mainshock, although some oblique, dip-slip (to the north), and pure thrust events near the epicenter were also observed. No spatiotemporal pattern or depth-latitude trend emerged across the ∼500 km fault. All aftershocks were shallower (median depth: 9 km) than the mainshock at ∼20 km.

Discussion and Conclusion

Teleseismic backprojection revealed that the rupture transitioned from subshear (stage-1) to supershear (stage-2), reaching a peak speed of >∼5.3 km/s ($1.6V_S$). During the supershear phase, the rupture first accelerated through the unstable regime (V_S to $\sqrt{2}V_S$), then entered the stable regime ($\sqrt{2}V_S$ to V_P) before decelerating slightly and terminating after 80 s, still supershear (Fig. 2d). It was the fastest large-earthquake rupture of the past 15 yr compared to the speeds obtained in a systematic backprojection analysis (Vera *et al.*, 2024), with a speed comparable to the 2001 Kunlunshan and 2002 Denali earthquakes, which also reached velocities above 5 km/s (Walker and Shearer, 2009).

The interpretation of stable supershear rupture depends on the depth and velocity model used to estimate shear wave speed. Here, we assumed the shear wave speed averaged along the rupture plane. If instead the maximum shear speed were used, the peak rupture speed would fall just below the stable supershear threshold (Fig. 2d). However, our rupture speed estimate is averaged from the epicenter, such that, given the subshear start, the instantaneous velocity during early stage-2 was likely higher. We therefore interpret the peak rupture speed as very likely within the stable supershear range.

Although the 2018 Palu earthquake was supershear from early on and exhibited unstable rupture behavior (Bao *et al.*, 2019), the Myanmar event transitioned to supershear only in its second half (stage-2), yet propagated over a 225 km segment at supershear speed. This delayed transition suggests lower initial shear stress in stage-1 compared to stage-2. Historical seismicity supports this (Fig. 2, inset): stage-1 (partially) overlaps the 1946 M 7.8 and 1956 M 7.0 rupture zones, whereas stage-2 initiated within the Sagaing fault seismic gap, where greater strain had accumulated. Supershear ruptures typically occur on long, simple strike-slip faults under uniform high stress (Bouchon *et al.*, 2010). Our remote-sensing image analysis of this segment revealed nearly uniform coseismic displacements between ∼21° and 19° N, consistent with conditions favoring supershear propagation.

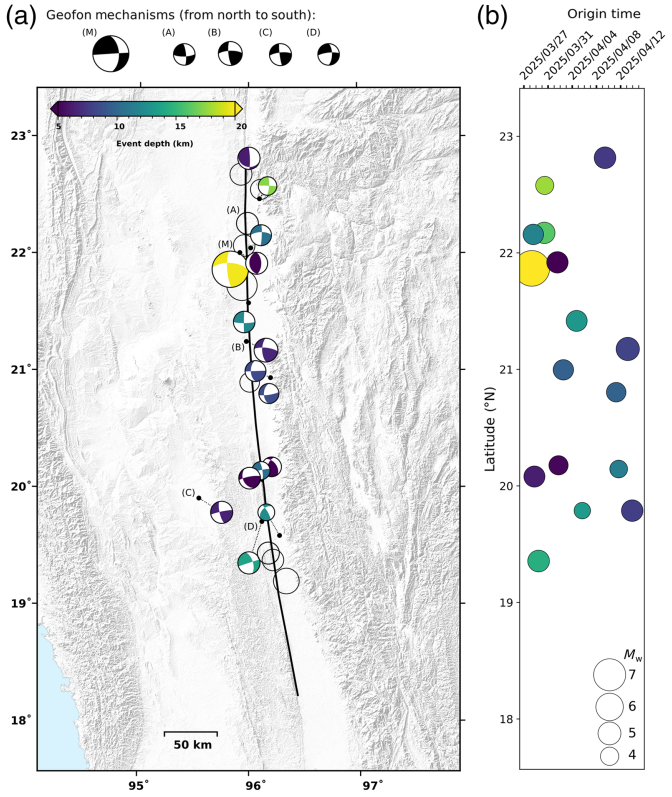

Figure 5. (a) Centroid Moment Tensor (CMT) inversion results for the mainshock and aftershocks from 28 April until 14 April 2025. Inversion results of this study are shown color coded by depth, with GEOFON catalog moment tensors in black at the top of the figure for comparison. Displayed are the double-couple (DC) components, with colored focal mechanism plots plotted at their derived centroid locations. The small black dots indicate the GEOFON catalog locations. Unfilled larger circles denote $M > 4$ aftershocks for which data quality was insufficient to obtain a stable CMT solution. The black line shows the ruptured fault segment as mapped from Interferometric Synthetic Aperture Radar (InSAR). (b) Temporal evolution of the aftershock sequence: latitude plotted over time, with symbol sizes scaled by magnitude and color coded by depth as in panel (a).

Supershear ruptures can generate strong ground shaking and damage from Mach wavefronts, with severity depending on rupture speed (e.g., Dunham and Bhat, 2008); synthetic seismogram envelopes from our preferred PDR model predict this effect (Fig. S10). Observed Mach wavefronts in Love waves at regional to teleseismic distances confirm this. Strong oblique radiation likely contributed to damage in Bangkok, over 1000 km from the epicenter and ~650 km from the rupture termination. The PDR model also predicts enhanced shear-wave energy in southwestern and southeastern directions (Fig. S10).

Station NPW recorded a displacement step of −13, 160, and 6 cm in the east, north, and up directions, respectively (Lai *et al.*, 2025). Located 2.6 km west of the fault trace, near cross-fault profile P7 (Fig. 4a,b), the 160 cm horizontal offset corresponds to about one-third of the ~5 m total offset measured on P7 by Sentinel-2 (Fig. 4c). Both Sentinel-1 and Sentinel-2 offset maps also showed asymmetric surface displacement, with greater southward motion east of the fault (Fig. 4, Fig. S2). Rectangular dislocation modeling assuming elastic conditions suggest that this asymmetry results from the curved and likely east-dipping geometry of the Sagaing fault (Fig. S9), which also could account for the asymmetric PDR model misfit. An east-dipping fault dip for the northern segments, with a transition to steeper dips in the south was inferred by other early studies on the Myanmar earthquake (Inoue *et al.*, 2025; Ye *et al.*, 2025).

The unusually low number of $M > 4$ aftershocks, especially along the southern rupture segment, further supports a supershear rupture. Supershear earthquakes often show reduced on-fault aftershock activity but may trigger clustering on secondary structures (Bouchon and Karabulut, 2008). The smooth, efficient energy release for a supershear rupture likely discharged most stress along the main fault, limiting aftershocks. Although we identified only one clear off-fault aftershock, several non-strike-slip mechanisms suggest activation of off-fault structures.

The rupture length is longer than expected for an M_w 7.7 strike-slip earthquake from scaling relations (e.g., Blaser *et al.*, 2010), where rupture lengths are generally on the order of 150–200 km, but not unusual. For instance, the 2023 M_w 7.7 Türkiye mainshock propagated over ~500 km (Petersen *et al.*, 2023). The large rupture length implies a moderate average slip, as inferred from the PDR inversion (about 3 m) because the total earthquake potency is distributed over a large fault plane.

Taken together, the exceptionally straight, elongated fault geometry; nearly uniform, southward-directed coseismic offsets; unusually low number of aftershocks; clear supershear rupture images from wide-azimuth multiarray backprojection; Mach-cone signatures; and PDR inversion validation including seismic and geodetic observations indicate that the 2025 Myanmar earthquake started as a bilateral, subshear rupture, but its southern branch transitioned to a sustained, likely stable, supershear rupture in the Sagaing fault seismic gap.

Data and Resources

European Integrated Data Archive (EIDA) (https://www.orfeus-eu.org/data/eida/) and National Science Foundation (NSF)–SAGE data center (https://ds.iris.edu/ds/nodes/dmc/data/types/waveform-data/) provided access to seismic data

for backprojection, Mach-cone analysis, and pseudodynamic rupture (PDR) inversion; see supplement for networks used. Hi-net data were downloaded from Natural Research Institute for Earth Science and Disaster Prevention (NIED). Aftershocks after four weeks (GEOFON catalog): https://geofon.gfz.de/fdsnws/event/1/query?format=text&starttime=2025-03-28T00:00:00.000Z&endtime=2025-04-25T23:59:59.999Z&minlatitude=15.75&maxlatitude=25.25&minlongitude=90.67&maxlongitude=101.47&. The authors used Copernicus Sentinel-1 and Sentinel-2 and Advanced Land Observation Satellite (ALOS)-2 ScanSAR satellite imagery, provided by Copernicus/ESA and the G-Portal data service of JAXA, respectively. PDR inversions utilized *pyrocko* routines (Heimann *et al.*, 2017). See supplement for citations of software used in the analysis of satellite data. All websites were last accessed in May 2025. The supplemental material includes additional figures, tables, and movies, providing more detailed insights into the data processing and results.

Declaration of Competing Interests

The authors acknowledge that there are no conflicts of interest recorded.

Acknowledgments

The authors thank the staff from the Department of Meteorology and Hydrology in Naypyitaw for keeping the stations of the MM network and the GE.NPW station operational. The authors thank T. Dahm for his guidance in setting up the pseudodynamic rupture (PDR) inversion. B. S. L. received funding from the National Agency for Research and Development (ANID; Scholarship Program: DOCTORADO BECAS CHILE 2023-72230401).

References

Bao, H., J.-P. Ampuero, L. Meng, E. J. Fielding, C. Liang, C. W. Milliner, T. Feng, and H. Huang (2019). Early and persistent supershear rupture of the 2018 magnitude 7.5 Palu earthquake, *Nature Geosci.* **12,** 200–205.

Blaser, L., F. Krüger, M. Ohrnberger, and F. Scherbaum (2010). Scaling relations of earthquake source parameter estimates with special focus on subduction environment, *Bull. Seismol. Soc. Am.* **100,** no. 6, 2914–2926.

Bouchon, M., and H. Karabulut (2008). The aftershock signature of supershear earthquakes, *Science* **320,** no. 5881, 1323–1325.

Bouchon, M., H. Karabulut, M.-P. Bouin, J. Schmittbuhl, M. Vallée, R. Archuleta, S. Das, F. Renard, and D. Marsan (2010). Faulting characteristics of supershear earthquakes, *Tectonophysics* **493,** nos. 3/4, 244–253.

Bradley, K., and J. Hubbard (2025). Remarkable video captures fault slip in the Myanmar earthquake, *Earthq. Insights* doi: 10.62481/01cd039c.

Burridge, R., G. Conn, and L. Freund (1979). The stability of a rapid mode II shear crack with finite cohesive traction, *J. Geophys. Res.* **84,** no. B5, 2210–2222.

Crosetto, S., I. M. Watkinson, S. Min, E. Falcucci, S. Gori, and P. S. Thein (2019). Searching for the 1912 Maymyo earthquake: New evidence from paleoseismic investigations along the Kyaukkyan fault, Myanmar, *Quat. Int.* **532,** 75–86.

Curray, J. R. (2005). Tectonics and history of the Andaman Sea region, *J. Asian Earth Sci.* **25,** no. 1, 187–232.

Dahm, T., S. Heimann, M. Metz, and M. P. Isken (2021). A self-similar dynamic rupture model based on the simplified wave-rupture analogy, *Geophys. J. Int.* **225,** no. 3, 1586–1604, doi: 10.1093/gji/ggab045.

Dunham, E. M., and H. S. Bhat (2008). Attenuation of radiated ground motion and stresses from three-dimensional supershear ruptures, *J. Geophys. Res.* **113,** no. B8, doi: 10.1029/2007jb005182.

Heimann, S., M. Isken, D. Kühn, H. Sudhaus, A. Steinberg, H. Vasyura-Bathke, S. Daout, S. Cesca, and T. Dahm (2018). Grond—A probabilistic earthquake source inversion framework, doi: 10.5880/GFZ.2.1.2018.003.

Heimann, S., M. Kriegerowski, M. Isken, S. Cesca, S. Daout, F. Grigoli, H. Sudhaus, H. Vasyura-Bathke, T. Willey, and T. Dahm (2017). Pyrocko—An open-source seismology toolbox and library, doi: 10.5880/GFZ.2.1.2017.001.

Hurukawa, N., and P. Maung Maung (2011). Two seismic gaps on the Sagaing fault, Myanmar, derived from relocation of historical earthquakes since 1918, *Geophys. Res. Lett.* **38,** no. 1, doi: 10.1029/2010GL046099.

Inoue, N., R. Yamaguchi, Y. Yagi, R. Okuwaki, E. Bogdan, and T. Tadapansawut (2025). A multiple asymmetric bilateral rupture sequence derived from the peculiar tele-seismic P-waves of the 2025 Mandalay, Myanmar earthquake, *Seismica* **4,** no. 1, doi: 10.26443/seismica.v4i1.1691.

Jónsson, S., H. Zebker, P. Segall, and F. Amelung (2002). Fault slip distribution of the 1999 M_w 7.1 Hector Mine, California, earthquake, estimated from satellite radar and GPS measurements, *Bul. Seismol. Soc. Am.* **92,** 1377–1389.

Lai, S.-T., K. M. Oo, Y. M. M. Htwe, T. Yi, H. H. Than, O. Than, Z. Min, T. M. Oo, P. M. Maung, D. Bindi, *et al.* (2025). Capacity building enables unique near-fault observations of the destructive 2025 M_w 7.7 Myanmar earthquake, *Earth Syst. Sci. Data Discuss.* **2025,** 1–23.

Latour, S., M. Lebihain, H. S. Bhat, C. Twardzik, Q. Bletery, K. W. Hudnut, and F. Passelègue (2025). Direct estimation of earthquake source properties from a single CCTV camera, doi: 10.48550/ARXIV.2505.15461.

Liang, C., Z. Liu, E. J. Fielding, and R. Bürgmann (2018). InSAR time series analysis of L-band wide-swath SAR data acquired by ALOS-2, *IEEE Trans. Geosci. Remote Sens.* **56,** no. 8, 4492–4506, doi: 10.1109/TGRS.2018.2821150.

Liang, Y., X. Yuan, B. Schurr, F. J. Tilmann, W. Li, and O. Than (2023). Lithospheric structure beneath northern Myanmar and surroundings from ambient noise tomography, *AGU Fall*

Meeting Abstracts, San Francisco, California, 11–15 December 2023, Number 452, S23G–0452.

Petersen, G. M., P. Büyükakpinar, F. O. Vera Sanhueza, M. Metz, S. Cesca, K. Akbayram, J. Saul, and T. Dahm (2023). The 2023 southeast Türkiye seismic sequence: Rupture of a complex fault network, *Seism. Rec.* **3,** no. 2, 134–143.

Robinson, D., S. Das, and M. Searle (2010). Earthquake fault superhighways, *Tectonophysics* **493,** nos. 3/4, 236–243.

Rosen, P. A., E. Gurrola, G. F. Sacco, and H. Zebker (2012). The InSAR scientific computing environment, *EUSAR 2012; 9th European Conference on Synthetic Aperture Radar*, Nuremberg, Germany, 23–26 April 2012, 730–733.

Searle, M., S. Noble, J. Cottle, D. Waters, A. Mitchell, T. Hlaing, and M. Horstwood (2007). Tectonic evolution of the Mogok metamorphic belt, Burma (Myanmar) constrained by U-Th-Pb dating of metamorphic and magmatic rocks, *Tectonics* **26,** no. 3, doi: 10.1029/2006TC002083.

Strozzi, T., A. Luckman, T. Murray, U. Wegmuller, and C. L. Werner (2002). Glacier motion estimation using SAR offset-tracking procedures, *IEEE Trans. Geosci. Remote Sens.* **40,** no. 11, 2384–2391, doi: 10.1109/TGRS.2002.805079.

Swe, W. (2013). The Sagaing fault of Myanmar: A brief overview, Commemoration of 9th Anniversary of MGS. Myanmar Geosciences Society, Yangon, Myanmar, 1–20.

Tin, T. Z. H., T. Nishimura, M. Hashimoto, E. O. Lindsey, L. T. Aung, S. M. Min, and M. Thant (2022). Present-day crustal deformation and slip rate along the southern Sagaing fault in Myanmar by GNSS observation, *J. Asian Earth Sci.* **228,** 105125.

Tun, S. T., and I. M. Watkinson (2017). The Sagaing fault, Myanmar, in *Myanmar: Geology, Resources and Tectonics*, A. J. Barber, K. Zaw, and M. J. Crow (Editors), The Geological Society of London, London, doi: 10.1144/M48.19.

Vera, F., F. Tilmann, and J. Saul (2024). A decade of short-period earthquake rupture histories from multi-array back-projection, *J. Geophys. Res.* **129,** no. 2, e2023JB027260, doi: 10.1029/2008JB005738.

Walker, K. T., and P. M. Shearer (2009). Illuminating the near-sonic rupture velocities of the intracontinental Kokoxili M_w 7.8 and Denali fault M_w 7.9 strike-slip earthquakes with global *P* wave back projection imaging, *J. Geophys. Res.* **114,** no. B2, doi: 10.1029/2008JB005738.

Wang, Y., K. Sieh, S. T. Tun, K.-Y. Lai, and T. Myint (2014). Active tectonics and earthquake potential of the Myanmar region, *J. Geophys. Res.* **119,** no. 4, 3767–3822.

Ye, L., T. Lay, and H. Kanamori (2025). The 28 March 2025 M_w 7.8 Myanmar earthquake: Preliminary analysis of an ~480 km long intermittent supershear rupture, *Seism. Rec.* **5,** no. 3, 260–269, doi: 10.1785/0320250021.

Zelenin, E., D. Bachmanov, S. Garipova, V. Trifonov, and A. Kozhurin (2021). The database of the active faults of Eurasia (AFEAD): Ontology and design behind the continental-scale dataset, *Earth Syst. Sci. Data Discuss.* **2021,** 1–20.

Manuscript received 16 June 2025
Published online 13 August 2025